

Towards an experimental von Kármán dynamo: numerical studies for an optimized design

Florent Ravelet, Arnaud Chiffaudel,* and François Daviaud

Service de Physique de l'État Condensé, DSM, CEA Saclay, CNRS URA 2464, 91191 Gif-sur-Yvette, France

Jacques Léorat†

LUTH, Observatoire de Paris-Meudon, 92195 Meudon, France

(To be published in Phys. Fluids: September 14, 2018)

Numerical studies of a kinematic dynamo based on von Kármán type flows between two counter-rotating disks in a finite cylinder are reported. The flow has been optimized using a water model experiment, varying the driving impellers configuration. A solution leading to dynamo action for the mean flow has been found. This solution may be achieved in VKS2, the new sodium experiment to be performed in Cadarache, France. The optimization process is described and discussed, then the effects of adding a stationary conducting layer around the flow on the threshold, on the shape of the neutral mode and on the magnetic energy balance are studied. Finally, the possible processes involved into kinematic dynamo action in a von Kármán flow are reviewed and discussed. Among the possible processes we highlight the joint effect of the boundary-layer radial velocity shear and of the Ohmic dissipation localized at the flow/outer-shell boundary.

PACS numbers: 47.65+a, 91.25.Cw

I. INTRODUCTION

In an electrically conducting fluid, kinetic energy can be converted into magnetic energy, if the flow is both of adequate topology and sufficient strength. This problem is known as the dynamo problem [1], and is a magnetic seed-field instability. The equation describing the behavior of the magnetic induction field \mathbf{B} in a fluid of resistivity η under the action of a velocity field \mathbf{v} writes in a dimensionless form:

$$\frac{\partial \mathbf{B}}{\partial t} = \nabla \times (\mathbf{v} \times \mathbf{B}) + \frac{\eta}{\mathcal{V}^* \mathcal{L}^*} \nabla^2 \mathbf{B} \quad (1)$$

where \mathcal{L}^* is a typical length scale and \mathcal{V}^* a typical velocity scale. In addition, one must take into account the divergence-free of \mathbf{B} , the electromagnetic boundary conditions and the Navier-Stokes equations governing the fluid motion, including the back-reaction of the magnetic field on the flow through the Lorentz force.

The magnetic Reynolds number $R_m = \mathcal{V}^* \mathcal{L}^* \eta^{-1}$, which compares the advection to the Ohmic diffusion, controls the instability. Although this problem is simple to set, it is still open. While some flows lead to the dynamo instability with a certain threshold R_m^c , other flows do not, and anti-dynamo theorems are not sufficient to explain this sensitivity to flow geometry [1]. The two recent experimental success of Karlsruhe and Riga [2, 3, 4, 5, 6] are in good agreement with analytical and numerical calculations [7, 8, 9, 10]; these two dynamos belong to the category of constrained dynamos: the flow

is forced in pipes and the level of turbulence remains low. However, the saturation mechanisms of a dynamo are not well known, and the role of turbulence on this instability remains misunderstood [11, 12, 13, 14, 15, 16, 17].

The next generation of experimental homogeneous unconstrained dynamos (still in progress, see for example Frick *et al.*, Shew *et al.*, Marié *et al.* and O'Connell *et al.* in the Cargèse 2000 workshop proceedings [18]) might provide answers to these questions. The VKS liquid-sodium experiment held in Cadarache, France [19, 20, 21] belong to this category. The VKS experiment is based on a class of flows called von Kármán type flows. In a closed cylinder, the fluid is inertially set into motion by two coaxial counterrotating impellers fitted with blades. This paper being devoted to the hydrodynamical and magnetohydrodynamical properties of the mean flow, let us first describe briefly the phenomenology of such mean flow. Each impeller acts as a centrifugal pump: the fluid rotates with the impeller and is expelled radially by centrifugal effect. To ensure mass conservation the fluid is pumped in the center of the impeller and recirculates near the cylinder wall. In the exact counterrotating regime, the mean flow is divided into two toric cells separated by an azimuthal shear layer. Such a mean flow has the following features, known to favor dynamo action: differential rotation, lack of mirror symmetry and presence of a hyperbolic stagnation point in the center of the volume. In the VKS experimental devices, the flow, inertially driven at kinetic Reynolds number up to 10^7 (see below), is highly turbulent. As far as full numerical MHD treatment of realistic inertially driven high-Reynolds-number flows cannot be carried out, this study is restricted to the kinematic dynamo capability of von Kármán mean flows.

Several measurements of induced fields have been performed in the first VKS device (VKS1) [20], in rather

*Electronic address: arnaud.chiffaudel@cea.fr

†Electronic address: Jacques.Leorat@obspm.fr

good agreement with previous numerical studies [22], but no dynamo was seen: in fact the achievable magnetic Reynolds number in the VKS1 experiment remained below the threshold calculated by Marié *et al.* [22]. A larger device —VKS2, diameter 0.6 m and 300 kW power supply— is under construction. The main generic properties of mean flow dynamo action have been highlighted by Marié *et al.* [22] on two different experimental von Kármán velocity fields. Furthermore, various numerical studies in comparable spherical flows confirmed the strong effect of flow topology on dynamo action [23, 28]. In the experimental approach, lots of parameters can be varied, such as the impellers blade design, in order to modify the flow features. In addition, following Bullard & Gubbins [24], several studies suggest to add a layer of stationary conductor around the flow to help the dynamo action. All these considerations lead us to consider the implementation of a static conducting layer in the VKS2 device and to perform a careful optimization of the mean velocity field by a kinematic approach of the dynamo problem.

Looking further towards the real VKS2 experiment, one should discuss the major remaining physical unexplored feature: the role of hydrodynamical turbulence. Such turbulence in an inertially-driven closed flow will be very far from homogeneity and isotropy. The presence of hydrodynamical small scale turbulence could act in two different ways: on the one hand, it may increase the effective magnetic diffusivity, inhibiting the dynamo action [25]. On the other hand, it could help the dynamo through small-scale α -effect [26]. Moreover, the presence of a turbulent mixing layer between the two counterrotating cells may move the instantaneous velocity field away from the time-averaged velocity field for large time-scales [27]. As the VKS2 experiment is designed to operate above the predicted kinematic threshold presented in this paper, it is expected to give an experimental answer to the question about the role of turbulence on the instability. Furthermore, if it exhibits dynamo, it will allow to study the dynamical saturation regime which is outside the present paper scope.

In this article, we report the optimization of the time-averaged flow in a von Kármán liquid sodium experiment. We design a solution which can be experimentally achieved in VKS2, the new device held in Cadarache, France. This solution particularly relies on the addition of a static conducting layer surrounding the flow. The paper is organized as follows. In Section II we first present the experimental and numerical techniques that have been used. In Section III, we present an overview of the optimization process which lead to the experimental configuration chosen for the VKS2 device. We study the influence of the shape of the impellers both on the hydrodynamical flow properties and on the onset of kinematic dynamo action. In Section IV, we focus on the understanding of the observed kinematic dynamo on a magnetohydrodynamical point of view: we examine the structure of the eigenmode and the effects of an outer

conducting boundary. Finally, in Section V, we review some possible mechanisms leading to kinematic dynamo action in a von Kármán flow and propose some conjectural explanations based on our observations.

II. EXPERIMENTAL AND NUMERICAL TOOLS

A. What can be done numerically

The bearing of numerical simulations in the design of experimental fluid dynamos deserves some general comments. Kinetic Reynolds numbers of such liquid sodium flows are typically 10^7 , well beyond any conceivable direct numerical simulation. Moreover, to describe effective MHD features, it would be necessary to manage very small magnetic Prandtl numbers, close to 10^{-5} , a value presently out of computational feasibility. Several groups are progressing in this way on model flows, for example with Large Eddy Simulations [15] which can reach magnetic Prandtl numbers as low as 10^{-2} – 10^{-3} . Another strong difficulty arises from the search of realistic magnetic boundary conditions treatment which prove in practice also to be difficult to implement, except for the spherical geometry.

An alternative numerical approach is to introduce a given flow in the magnetic induction equation 1 and to perform “kinematic dynamo” computations. This flow can be either analytical [8, 23], computed by pure hydrodynamical simulations (which may now be performed with Reynolds numbers up to a few thousands), or measured in laboratory water models [22, 28] by Laser Doppler velocimetry (LDV) or by Particle Imaging Velocimetry (PIV). Such measurements lead to a map of the time-averaged flow and to main properties of the fluctuating components: turbulence level, correlation times, etc... Kinematic dynamo computations have been successfully used to describe or optimize the Riga [7] and Karlsruhe [8] dynamo experiments.

We will follow here the kinematic approach using the time-averaged flow measured in a water model at realistic kinetic Reynolds number. Indeed, potentially important features such as velocity fluctuations will not be considered. Another strong limitation of our pragmatic kinematic approach is its linearity: computations may predict if an initial seed field grows, but the study of the saturation regime will rely exclusively on the results of the real MHD experiment VKS.

B. Experimental measurements

In order to measure the time-averaged velocity field — hereafter simply denoted mean field— we use a water-model experiment which is a half-scale model of the VKS2 sodium device. The experimental setup, measurement techniques, and methods are presented in detail in

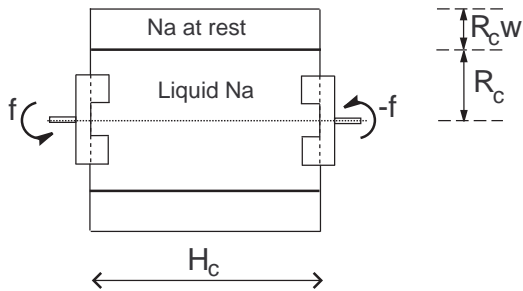


FIG. 1: Sketch of the VKS2 experiment. The container radius R_c is taken as unit scale. w is the dimensionless thickness of sodium at rest.

Refs. [22, 29]. However, we present below an overview of our experimental issues and highlight the evolutions with respect to those previous works.

We use water as working fluid for our study, noting that its hydrodynamical properties at 50°C (kinematic viscosity ν and density ρ) are very close to sodium properties at 120°C .

A sketch of the von Kármán experiments is presented in Fig. 1. The cylinder is of radius R_c and height $H_c = 1.8R_c$. In the following, all the spatial quantities are given in units of $R_c = \mathcal{L}^*$. The hydrodynamical time scale is based on the impeller driving frequency f : if \mathbf{V} is the measured velocity field for a driving frequency f , the dimensionless mean velocity field is thus $\mathbf{v} = (2\pi R_c f)^{-1} \mathbf{V}$.

The integral kinetic Reynolds number Re is typically 10^6 in the water-model, and 10^7 in the sodium device VKS2. The inertially driven flow is highly turbulent, with velocity fluctuations up to 40 percent of the maximum velocity [20, 22]. In the water model, we measure the time-averaged velocity field by Laser Doppler Velocimetry (LDV). Data are averaged over typically 300 disk rotation periods. We have performed measurements of velocity in several points for several driving frequencies: as expected for so highly turbulent a flow, the dimensionless velocity \mathbf{v} does not depend on the integral Reynolds number $Re = \mathcal{V}^* \mathcal{L}^* \nu^{-1}$ [30].

Velocity modulations at the blade frequency have been observed only in and very close to the inter-blade domains. These modulations are thus time-averaged and we can consider the mean flow as a solenoidal axisymmetric vector field [31]. So the toroidal part of the velocity field V_θ (in cylindrical coordinates) and the poloidal part (V_z, V_r) are independent.

In the water model experiment dedicated to the study reported in this paper, special care has been given to the measurements of velocity fields, especially near the blades and at the cylinder wall, where the measurement grid has been refined. The mechanical quality of the experimental setup ensures good symmetry of the mean velocity fields with respect to rotation of π around any diameter passing through the center of the cylinder (\mathcal{R}_π -

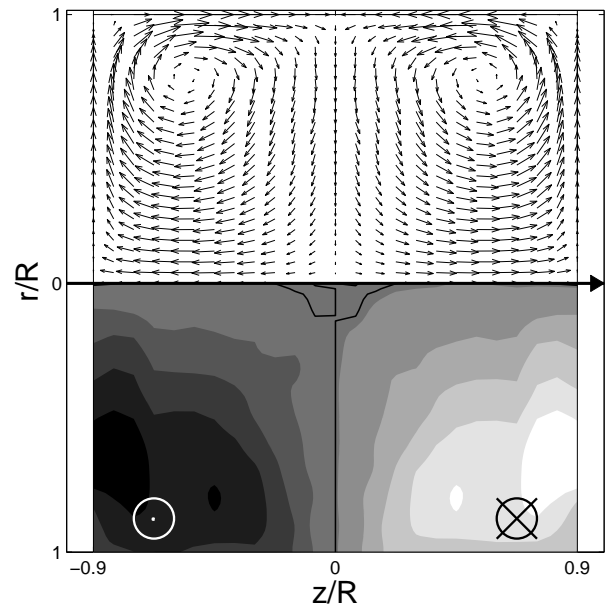


FIG. 2: Dimensionless mean velocity field measured by LDV and symmetrized for kinematic dynamo simulations. Cylinder axis is horizontal. Arrows correspond to poloidal part of the flow, color code to toroidal part. We use cylindrical coordinates (r, θ, z) , with origin at the center of the cylinder.

symmetry). The fields presented in this paper are thus symmetrized by \mathcal{R}_π with no noticeable changes in the profiles but with a slightly improved spatial signal-to-noise ratio. With respect to Ref. [22], the velocity fields are neither smoothed, nor stretched to different aspect ratios.

Fig. 2 shows the mean flow produced by the optimal impeller. The mean flow respects the phenomenology given in the Introduction: it is made of two toroidal cells separated by a shear layer, and two poloidal recirculation cells. High velocities are measured in the whole volume: the inertial stirring is actually very efficient. Typically, the average over the flow volume of the mean velocity field is of order of $0.3 \times (2\pi R_c f)$.

In addition to velocity measurements, we perform global power consumption measurements: torques are measured through the current consumption in the motors given by the servo drives and have been calibrated by calorimetry.

C. Kinematic dynamo simulations

Once we know the time-averaged velocity field, we integrate the induction equation using an axially periodic kinematic dynamo code, written by J. Léorat [32]. The code is pseudo-spectral in the axial and azimuthal directions whether radial dependence is treated by high-order finite difference scheme. The numerical resolution cor-

responds to a grid of 48 points in the axial direction, 4 points in the azimuthal direction (corresponding to wave numbers $m = 0, \pm 1$) and 51 points in the radial direction for the flow domain. This spatial grid is the common basis of our simulations and has been refined in some cases. The time scheme is second-order Adams-Bashforth with diffusive time unit $t_d = R_c^2 \eta^{-1}$. Typical time step is 5.10^{-6} and simulations are generally carried out over 1 time unit.

Electrical conductivity and magnetic permeability are homogeneous and the external medium is insulating. Implementation of the magnetic boundary conditions for a finite cylinder is difficult, due to the non-local character of the continuity conditions at the boundary of the conducting fluid. On the contrary, axially periodic boundary conditions write down easily, since the harmonic external field has then an analytical expression. We choose thus to look for axially periodic solutions, using a relatively fast code, which allows to perform parametric studies. To validate our choice, we compared our results with results from a finite cylinder code (F. Stefani, private communication) for some model flows and a few experimental flows. It happens that in all these cases, the periodic and the finite cylinder computations give comparable results. This remarkable agreement may be due to the peculiar flow and to the magnetic eigenmodes symmetries: we do not claim that it may be generalized to other flow geometries. Indeed, the numerical elementary box consists of two mirror-symmetric experimental velocity fields in order to avoid strong velocity discontinuities along z axis. The magnetic eigenmode could be either symmetric or antisymmetric towards this artificial mirror symmetry [33]. In the quasi totality of our simulations, the magnetic field is mirror-antisymmetric, and we verify that no axial currents cross the mirror boundary. The few exotic symmetric cases we encountered cannot be used for experiments optimization.

Further details on the code can be found in Ref. [32]. We use mirror-antisymmetric initial magnetic seed field optimized for fast transient [22]. Finally, we can act on the electromagnetic boundary conditions by adding a layer of stationary conductor of dimensionless thickness w , surrounding the flow exactly as in the experiment (Fig. 1). This extension is made keeping the grid radial resolution constant (51 points in the flow region).

III. OPTIMIZATION OF THE VKS EXPERIMENT

A. Optimization process

The goal of our optimization process is to find the impeller whose mean velocity field leads to the lowest R_m^c for the lowest power cost. We have to find a solution feasible in VKS2, *i.e.* with liquid sodium in a 0.6 m diameter cylinder with 300 kW power supply. We performed an iterative optimization loop: for a given configuration, we

measure the mean velocity field and the power consumption. Then we simulate the kinematic dynamo problem. We try to identify features favoring dynamo action and modify parameters in order to reduce the threshold and the power consumption and go back to the loop.

B. Impeller tunable parameters.

The impellers are flat disks of radius R fitted with 8 blades of height h . The blades are arcs of circle with a curvature radius C and are radial at the center of the disks. We use the angle $\alpha = \arcsin(\frac{R}{2C})$ to label the different curvatures (see Fig. 3). For straight blades $\alpha = 0$. By convention, we use positive values to label the direction corresponding to the case where the fluid is set into motion by the convex face of the blades. In order to study the opposite curvature ($\alpha < 0$) we just rotate the impeller in the other direction. The two counter-rotating impellers are separated by H_c , the height of the cylinder. We fixed the aspect ratio H_c/R_c of the flow volume to 1.8 as in VKS device. In practice we successively examine the effects of each parameter h , R and α on some global quantities characterizing the mean flow. We then varied the parameters one by one, until we found a relative optimum for the dynamo threshold. We tested 12 different impellers, named TMxx, with three radii ($R = 0.5, 0.75$ & 0.925), various curvature angles α and different blade heights h .

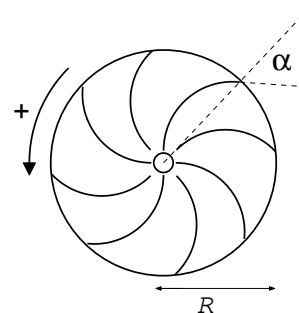


FIG. 3: Sketch of the impeller parameters. R is the dimensionless radius, α the blade curvature angle. The sign of α is determined by the sense of rotation: positive when rotated anticlockwise.

C. Global quantities and scaling relations

We know from empirical results [22, 23, 28] that the poloidal to toroidal ratio Γ of the flow has a great impact on the dynamo threshold. Moreover, a purely toroidal flow is unable of sustained dynamo action [34, 35], while it is possible for a purely poloidal flow [36, 37]. We also notice that, for a Ponomarenko flow, the pitch parameter plays a major role [7, 16, 17]. All these results lead us to

first focus on the ratio

$$\Gamma = \frac{\langle P \rangle}{\langle T \rangle}$$

where $\langle P \rangle$ is the spatially averaged value of the poloidal part of the mean flow, and $\langle T \rangle$ the average of the toroidal part.

Another quantity of interest is the velocity factor \mathcal{V} : the dimensionless maximum value of the velocity. In our simulations, the magnetic Reynolds number R_m is based on the velocity factor, *i.e.* on a typical *measured* velocity in order to take into account the stirring efficiency:

$$\mathcal{V} = \frac{\max(\|\mathbf{V}\|)}{2 \pi R_c f}$$

$$R_m = 2 \pi R_c^2 f \mathcal{V} / \eta$$

We also define a power coefficient K_p by dimensional analysis. We write the power \mathcal{P} given by a motor to sustain the flow as follows:

$$\mathcal{P} = K_p(Re, geometry) \rho R_c^5 \Omega^3$$

with ρ the density of the fluid and $\Omega = 2\pi f$ the driving pulsation. We have checked [29] that K_p does not depend on the Reynolds number Re as expected for so highly turbulent inertially driven flows [30].

The velocity factor measures the stirring efficiency: the greater \mathcal{V} , the lesser the rotation frequency needed to reach a given velocity. Besides, the lesser K_p , the lesser the power to sustain a given driving frequency. The dimensionless number which we need to focus on compares the velocity effectively reached in the flow to the power consumption. We call it the MaDo number:

$$\text{MaDo} = \frac{\mathcal{V}}{K_p^{1/3}}$$

The greater MaDo, the lesser the power needed to reach a given velocity (*i.e.* a given magnetic Reynolds number). The MaDo number is thus a hydrodynamical efficiency coefficient. To make the VKS experiment feasible at laboratory scale, it is necessary both to have great MaDo numbers and low critical magnetic Reynolds numbers R_m^c . The question laying under the process of optimization is to know if we could on the one hand find a class of impellers with mean flows exhibiting dynamo action, and on the other hand if we could increase the ratio MaDo/R_m^c . It means that we have to look both at the global hydrodynamical quantities and at the magnetic induction stability when varying the impellers tunable parameters h , R and α .

Fig. 4 presents MaDo for the whole set of impellers. For our class of impellers, the MaDo number remains of the same order of magnitude within $\pm 10\%$. Only the smallest diameter impeller ($R = 0.5$) exhibits a slightly higher value. In the ideal case of homogeneous isotropic

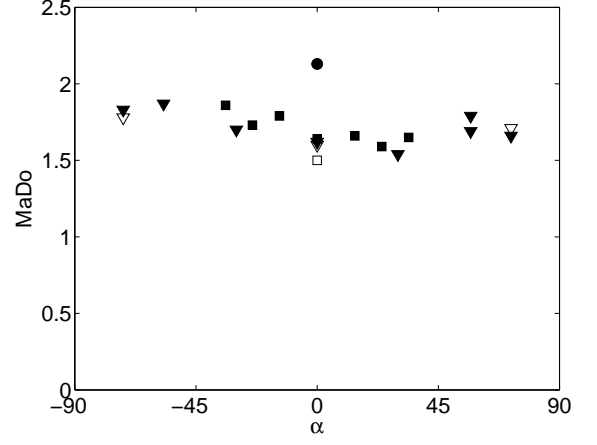


FIG. 4: MaDo number vs α for all the impellers we have tested. $R = 0.925$ (\blacktriangledown), $R = 0.75$ (\blacksquare) and $R = 0.5$ (\bullet). Closed symbols: $h = 0.2$. Open symbols: $h \leq 0.1$

turbulence, far from boundaries, we can show that what we call the MaDo number is related to the Kolmogorov constant $C_K \simeq 1.5$ [38]. The Kolmogorov constant is related to the kinetic energy spatial spectrum:

$$E(k) = C_K \epsilon^{2/3} k^{-5/3}$$

where ϵ is the massic dissipated power, and k the wave number. If we assume that ϵ is homogeneous — \mathcal{P} being the total dissipated power we measure— we have:

$$\epsilon = \frac{\mathcal{P}}{\rho \pi R_c^2 H_c}$$

Using the definition

$$\frac{1}{2} \langle v^2 \rangle = \int E(k) dk$$

and assuming $\frac{1}{2} \langle v^2 \rangle \simeq \frac{1}{2} \mathcal{V}^2$ and using the steepness of the spectrum, we obtain:

$$E(k_0) = \frac{1}{3} \mathcal{V}^2 k_0^{-1}$$

with $k_0 = 2\pi/R_c$ the injection scale. Then the relation between the MaDo number and C_K would be:

$$\text{MaDo}^2 \simeq 3\pi^{-4/3} \left(\frac{H_c}{R_c}\right)^{-2/3} C_K \simeq 0.44 C_K$$

i.e., with $C_K = 1.5$, we should have, for homogeneous isotropic turbulence $\text{MaDo} \simeq 0.81$. In our closed system with blades, we recover the same order of magnitude, and the fact that MaDo does merely not depend on the driving system. Thus, there is no obvious optimum for the hydrodynamical efficiency. Between various impellers producing dynamo action, the choice will be dominated by the value of the threshold R_m^c .

Let us first get rid of the effect of the blade height h . The power factor K_p varies quasi-linearly with h . As MaDo is almost constant, smaller h impellers require higher rotation frequencies, rising technical difficulties. We choose $h = 0.2$, a compromise between stirring efficiency and the necessity to keep the free volume sufficiently large.

D. Influence of the poloidal/toroidal ratio Γ

In our cylindrical von Kármán flow without conducting layer ($w = 0$), there seems to be an optimal value for Γ close to 0.7. Since the mean flow is axisymmetric and divergence-free, the ratio Γ can be changed numerically by introducing an arbitrary multiplicative factor on, say, the toroidal part of the velocity field. In the following, Γ_0 stands for the experimental ratio for the measured mean velocity field, whereas Γ stands for the numerically adjusted ratio.

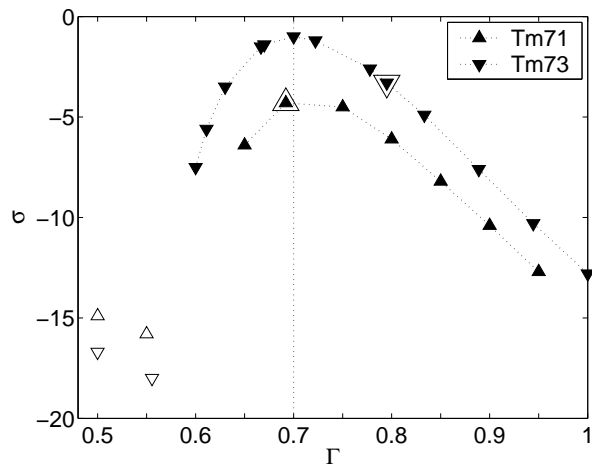


FIG. 5: Magnetic energy growth rate σ vs. numerical ratio Γ . $R_m = 100$, $w = 0$. Simulations performed for two different mean velocity fields (impellers TM71 (\blacktriangle) and TM73 (\blacktriangledown) of radius $R = 0.75$). Larger symbols correspond to natural Γ_0 of the impeller. Vertical dashed line corresponds to optimal $\Gamma = 0.7$. Closed symbols stand for stationary regimes, whereas open symbols stand for oscillating regimes for $\Gamma \lesssim 0.6$.

In Fig. 5, we plot the magnetic energy growth rate σ (twice the magnetic field growth rate) for different values of Γ , for magnetic Reynolds number $R_m = 100$ and without conducting layer ($w = 0$). The two curves correspond to two different mean velocity fields which have been experimentally measured in the water model (they correspond to the TM71 and TM73 impellers, see table I for their characteristics). We notice that the curves show the same bell shape with maximum growth rate at $\Gamma \simeq 0.7$, which confirms the results of Ref. [22].

For $\Gamma \lesssim 0.6$, oscillating damped regimes (open symbols in Fig. 5) are observed. We plot the temporal evolution

of the magnetic energy in corresponding case in Fig. 6: these regimes are qualitatively different from the oscillating regimes already found in [22] for *non* \mathcal{R}_π -symmetric $\Gamma = 0.7$ velocity fields, consisting of one mode with a complex growth rate: the magnetic field is a single traveling wave, and the magnetic energy, integrated over the volume, evolves monotonically in time.

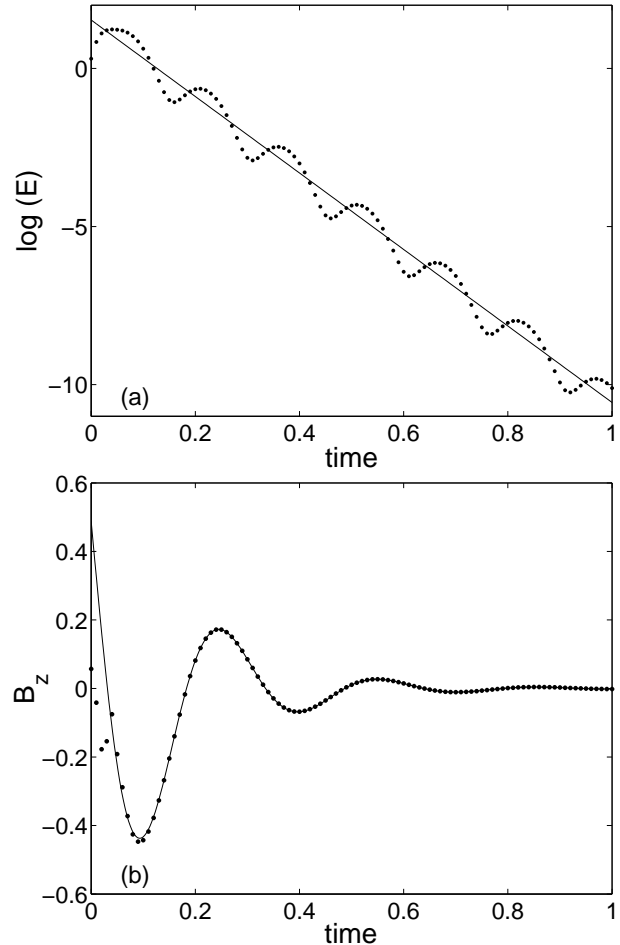


FIG. 6: Typical damped oscillating regime for impeller TM70 at $\Gamma = 0.5$, $w = 0$, $R_m = 140$. (a): temporal evolution of the magnetic energy $E = \int \mathbf{B}^2$. Straight line is a linear fit of the form $E(t) = E_0 \exp(\sigma t)$ and gives the temporal growth rate $\sigma = -12.1$. (b): temporal evolution of the z component of \mathbf{B} at the point $r = 0.4, \theta = 0, z = -0.23$ with a nonlinear fit of the form: $B_z(t) = a \exp(\sigma t/2) \cos(\omega t + \phi)$ which gives $\sigma = -12.2$ and $\omega = 20.7$.

In our case, the velocity field is \mathcal{R}_π -symmetric. It is known that symmetries strongly constrain the nature of eigenvalues and eigenmodes of linear stability problems. Due to \mathcal{R}_π -symmetry invariance of the evolution operator for the magnetic field, two type of solutions are allowed [33]:

- One \mathcal{R}_π -symmetric eigenmode with a real eigenvalue. The corresponding bifurcation is steady.

- Two eigenmodes images one of the other by \mathcal{R}_π , associated with complex-conjugate eigenvalues.

For $\Gamma \gtrsim 0.6$, we always observed stationary regimes. Otherwise, for $\Gamma \lesssim 0.6$, starting the temporal integration with an initial condition for the magnetic field which has non vanishing projection on both eigenmodes, we obtain a mix of two modes with complex-conjugate growth rates and the magnetic energy decays exponentially while pulsating (Fig. 6). The same feature has been reported for analytical “ $s_2^0 t_2^0$ – like flows” in a cylindrical geometry with a Galerkin analysis of neutral modes and eigenvalues for the induction equation [39]. A major interest of the latter method is that it gives the structure of the modes: one mode is localized near one impeller and rotates with it, the other being localized and rotating with the other impeller. Growing oscillating dynamos are rare in our system: a single case has been observed, for TM71(–) ($\Gamma_0 = 0.53$) with a $w = 0.4$ conducting layer at $R_m = 215$ ($R_m^c = 197$, see table I). Such high a value for the magnetic Reynolds number is out of the scope of our experimental study, and is close to the practical upper limit of the numerical code.

Experimental dynamo action will thus be searched in the stationary regimes domain $\Gamma \gtrsim 0.6$. Without conducting layer, we have to look for the optimal impeller around $\Gamma_0 \simeq 0.7$.

E. Effects of the impeller radius R

One could *a priori* expect that a very large impeller is favorable to the hydrodynamical efficiency. This is not the case. For impellers with straight blades, MaDo slightly decreases with R : for respectively $R = 0.5$, 0.75 and 0.925 , we respectively get $\text{MaDo} = 2.13$, 1.64 and 1.62 . This tendency is below the experimental error. We thus consider that MaDo does not depend on the impeller.

Nevertheless one should not forget that \mathcal{V} varies quasi-linearly with impeller radius R : if the impeller becomes smaller it must rotate faster to achieve a given value for the magnetic Reynolds number, which may again cause mechanical difficulties. We do not explore radii R smaller than 0.5 .

Concerning the topology of the mean flow, there is no noticeable effects of the radius R on the poloidal part. We always have two toric cells of recirculation, centered at a radius r_p close to 0.75 ± 0.02 and almost constant for all impellers (see right part of Fig. 7). The fluid is pumped to the impellers for $0 < r < r_p$ and is reinjected in the volume $r_p < r < 1$. This can be interpreted as a geometrical constraint to ensure mass conservation: the circle of radius $r = \frac{\sqrt{2}}{2}$ (very close to 0.75) separates the unit disk into two regions of same area.

The topology of the toroidal part of the mean flow now depends on the radius of the impeller. The radial profile of v_θ shows stronger departure from solid-body rotation

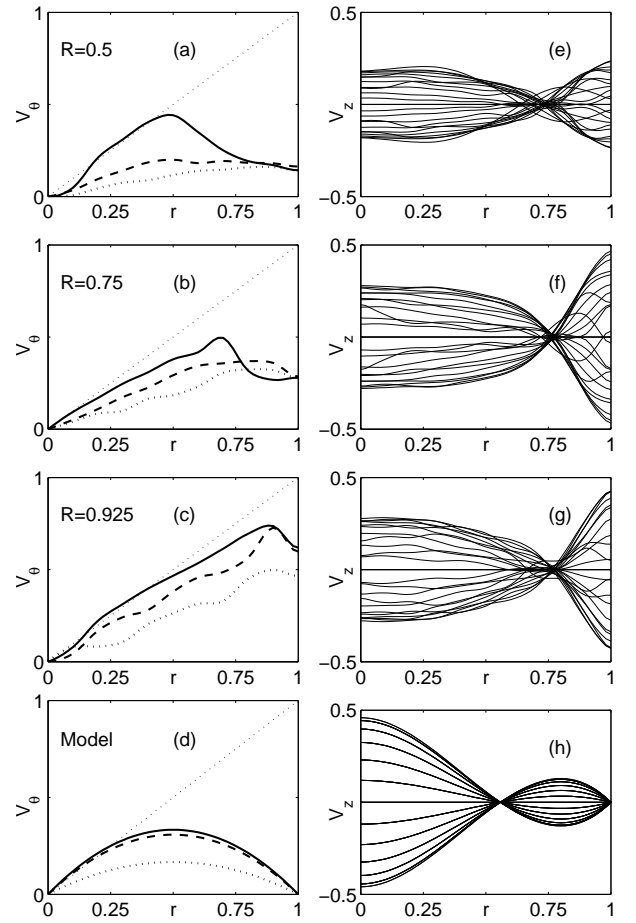


FIG. 7: Radial profiles of toroidal velocity v_θ ((a)–(d)) for $z = 0.3$ (dotted line), 0.675 (dashed line), & 0.9 (solid line); and axial velocity v_z ((e)–(h)) for various equidistant z between the two rotating disks. From top to bottom: experimental flow for (a–e): $R = 0.5$, (b–f): $R = 0.75$, (c–g): $R = 0.925$ impeller and (d–h): model analytical flow given by equations (1) (see discussion below p. 15).

for smaller R (left part of Fig. 7): this will be emphasized in the discussion. We performed simulations for three straight blades impellers of radii $R = 0.5$, $R = 0.75$ and $R = 0.925$; without conducting shell ($w = 0$) and with a conducting layer of thickness $w = 0.4$. We have integrated the induction equation for the three velocity fields numerically set to various Γ and compared the growth rates. The impeller of radius $R = 0.75$ close to the radius of the center of the poloidal recirculation cells systematically gets greatest growth rate. So, this radius $R = 0.75$ has been chosen for further investigations.

F. Seek for the optimal blade curvature

The hydrodynamical characteristics of the impellers of radius $R = 0.75$ are given in table I. For increasing blade curvature the average value of the poloidal velocity $\langle P \rangle$

increases while the average value of the toroidal velocity $\langle T \rangle$ decreases: the ratio Γ_0 is a continuous growing function of curvature α (Fig. 8). A phenomenological explanation for $\langle T \rangle$ variation can be given. The fluid pumped by the impeller is centrifugally expelled and is constrained to follow the blades. So, it exits the impeller with a velocity almost tangent to the blade exit angle α . Thus, for $\alpha < 0$ (resp. $\alpha > 0$), the azimuthal velocity is bigger (resp. smaller) than the solid body rotation. Finally, it is possible to adjust Γ_0 to a desired value by choosing the good curvature α , in order to lower the threshold for dynamo action.

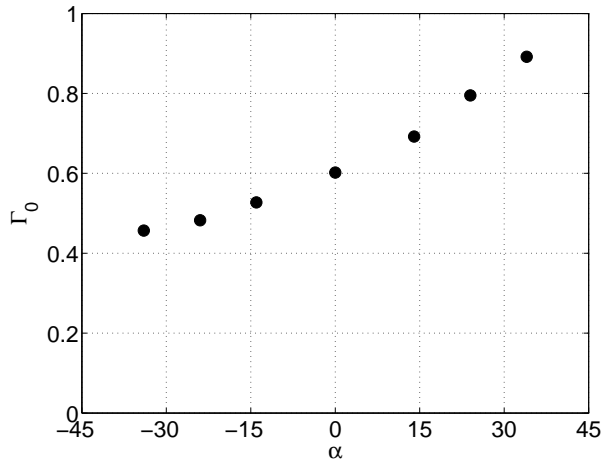


FIG. 8: Γ_0 vs α for four impellers of radius $R = 0.75$ rotated in positive and negative direction (see Table I).

Without conducting shell, the optimal impeller is the TM71 ($\Gamma_0 = 0.69$). But its threshold $R_m^c = 179$ cannot be achieved in the VKS2 experiment. So, we now have to find another way to reduce R_m^c , the only relevant factor for the optimization.

G. Optimal configuration to be tested in the VKS2 sodium experiment

As in the Riga experiment [4, 7], and as in numerical studies of various flows [24, 42, 43], we consider a stationary layer of fluid sodium surrounding the flow. This significantly reduces the critical magnetic Reynolds number, but also slightly shifts the optimal value for Γ . We have varied w between $w = 0$ and $w = 1$; since the experimental VKS2 device is of fixed overall size (diameter 0.6 m), the flow volume decreases while increasing the static layer thickness w . A compromise between this constraint and the effects of increasing w has been found to be $w = 0.4$ and we mainly present here results concerning this value of w . In Fig. 9, we compare the bell-shaped curves obtained by numerical variation of the ratio Γ for the same impeller at the same R_m , in the case $w = 0$, and $w = 0.4$. The growth rates are much higher for

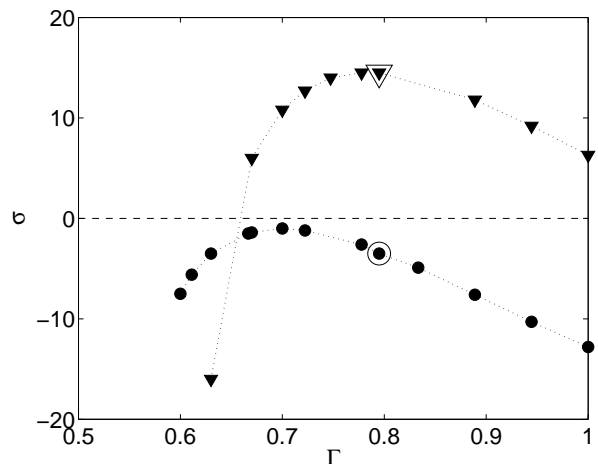


FIG. 9: Shift in the optimal value of Γ when adding a conducting layer. Magnetic energy growth rate σ vs. Γ for $w = 0$ (●) and $w = 0.4$ (▼). Impeller TM73, $R_m = 100$. Larger symbols mark the natural Γ_0 of the impeller.

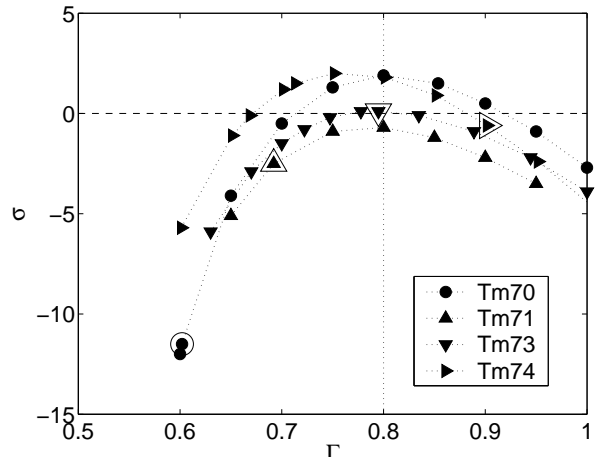


FIG. 10: Growth rate σ of magnetic energy vs numerical ratio Γ . $R_m = 43$, $w = 0.4$ for 4 different $R = 0.75$ impellers: TM70 (●), TM71 (▲), TM73 (▼) and TM74 (►). Larger symbols mark the natural Γ_0 of each impeller.

$w = 0.4$, and the peak of the curve shifts from 0.7 to 0.8. We have performed simulations for four different velocity fields (Fig. 10), for $w = 0.4$ at $R_m = 43$: the result is very robust, the four curves being very close.

In Fig. 11, we plot the growth rates σ of the magnetic energy simulated for four real mean velocity fields at various R_m and for $w = 0.4$. The impeller TM73 was designed to create a mean velocity field with $\Gamma_0 = 0.80$. It appears to be the best impeller, with a critical magnetic Reynolds number of $R_m^c = 43$. Its threshold is divided by a factor 4 when adding a layer of stationary conductor. This configuration (TM73, $w = 0.4$) will be the first one tested in the VKS2 experiment. The VKS2 ex-

Impeller	$\alpha^{(0)}$	$\langle P \rangle$	$\langle T \rangle$	$\Gamma_0 = \frac{\langle P \rangle}{\langle T \rangle}$	$\langle P \rangle \cdot \langle T \rangle$	$\langle H \rangle$	\mathcal{V}	K_p	$MaDo$	$R_m^c (w=0)$	$R_m^c (w=0.4)$
TM74(-)	-34	0.15	0.34	0.46	0.052	0.43	0.78	0.073	1.86	n.i.	n.i.
TM73(-)	-24	0.16	0.34	0.48	0.055	0.41	0.72	0.073	1.73	n.i.	n.i.
TM71(-)	-14	0.17	0.33	0.53	0.057	0.49	0.73	0.069	1.79	n.i.	197 (o)
TM70	0	0.18	0.30	0.60	0.056	0.47	0.65	0.061	1.64	(1)	(1)
TM71	+14	0.19	0.28	0.69	0.053	0.44	0.64	0.056	1.66	179	51
TM73	+24	0.20	0.25	0.80	0.051	0.44	0.60	0.053	1.60	180	43
TM74	+34	0.21	0.24	0.89	0.050	0.44	0.58	0.043	1.65	∞	44

TABLE I: Global hydrodynamical dimensionless quantities (see text for definitions) for the radius $R = 0.75$ impeller family, rotating anticlockwise (+), or clockwise (-) (see Fig. 3). The last two columns present the thresholds for kinematic dynamo action with ($w = 0.4$) and without ($w = 0$) conducting layer. Optimal values appear in bold font. Most negative curvatures have not been investigated (n.i.) but TM71(-), which presents oscillatory (o) dynamo instability for $R_m^c = 197$ with $w = 0.4$. (1): TM70 impeller ($\Gamma_0 = 0.60$) has a tricky behavior exchanging stability between steady modes, oscillatory modes and a singular mode mirror-symmetric with respect to the periodization introduced along z and thus not physically relevant.

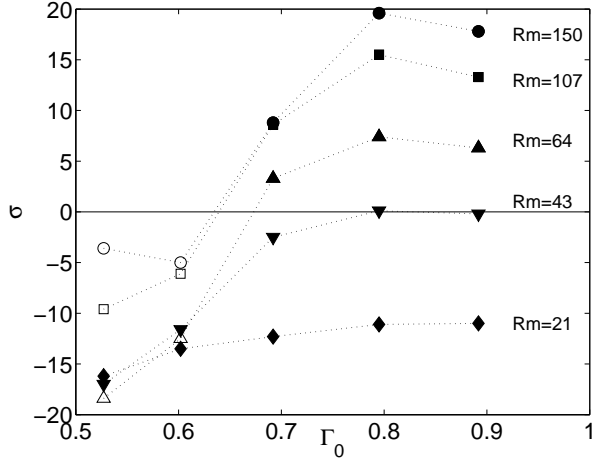


FIG. 11: Growth rate σ vs natural ratio Γ_0 for five impellers at various R_m and $w = 0.4$. From left to right: TM71(-) with $\Gamma_0 = 0.53$, TM70 ($\Gamma_0 = 0.60$), TM71 ($\Gamma_0 = 0.69$), TM73 ($\Gamma_0 = 0.80$), TM74 ($\Gamma_0 = 0.89$), see also table I). Closed symbols: stationary modes. Open symbols: oscillating modes.

periment will be able to reach the threshold of kinematic dynamo action for the mean part of the flow. Meanwhile, turbulence level will be high and could lead to shift or even disappearance of the kinematic dynamo threshold. In Section IV, we examine in details the effects of the boundary conditions on TM73 kinematic dynamo.

H. Role of flow helicity vs. Poloidal/Toroidal ratio

Most large scale dynamos known are based on helical flows [1, 40]. As a concrete example, while successfully optimizing the Riga dynamo experiment, Stefani *et al.* [7] noticed that the best flows were helicity maximizing. The first point we focused on during our optimization process, *i.e.*, the existence of an optimal value for Γ , leads us to

address the question of the links between Γ and mean helicity $\langle H \rangle$. In our case, for aspect ratio $H_c/R_c = 1.8$ and impellers of radius $R = 0.75$, the mean helicity at a given rotation rate $\langle H \rangle = \int \mathbf{v} \cdot (\nabla \times \mathbf{v}) r dr dz$ does not depend on the blade curvature (see Table I). Observation of Fig. 12 also reveals that the dominant contribution in the helicity scalar product is the product of the toroidal velocity ($v_\theta \propto \langle T \rangle$) by the poloidal recirculation cells vorticity ($(\nabla \times \mathbf{v})_\theta \propto \langle P \rangle$). We can therefore assume the scaling $\langle H \rangle \propto \langle P \rangle \langle T \rangle$, which is consistent with the fact that the product $\langle P \rangle \langle T \rangle$ and $\langle H \rangle$ are both almost constant (Table I).

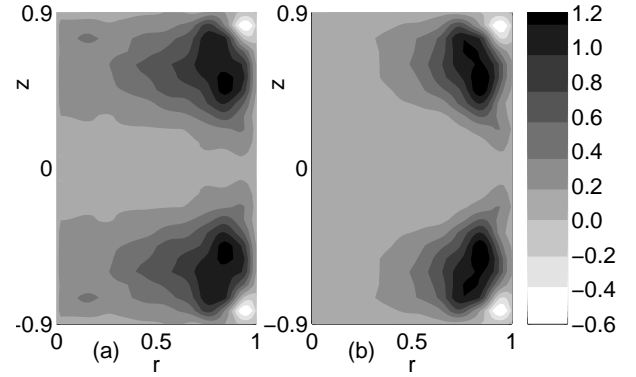


FIG. 12: Isocontour of kinetic helicity $H = \mathbf{v} \cdot (\nabla \times \mathbf{v})$ for TM73 velocity field. (a): total helicity. (b): azimuthal contribution $v_\theta \cdot (\nabla \times \mathbf{v})_\theta$ is dominant.

To compare the helicity content of different flows, we now consider the mean helicity at a given R_m , $\langle H \rangle / \mathcal{V}^2$, more relevant for the dynamo problem. Figure 13 presents $\langle H \rangle / \mathcal{V}^2$ versus Γ_0 for all $h = 0.2$ impellers. The $R = 0.75$ family reaches a maximum of order of 1 for $\Gamma_0 \simeq 0.9$. This tendency is confirmed by the solid curve which stands for a numerical variation of Γ for TM73 velocity field and is maximum for $\Gamma = 1$. Besides, even if $R = 0.925$ impellers give reasonably high values of helicity

ity near $\Gamma = 0.5$, there is an abrupt break in the tendency for high curvature: TM60 (see Ref. [22]) exhibits large $\Gamma_0 = 0.9$ but less helicity than TM74. Inset in Fig. 13 highlights this optimum for $\langle H \rangle / \mathcal{V}^2$ versus impeller radius R . This confirms the impeller radius $R = 0.75$ we have chosen during the optimization described above.

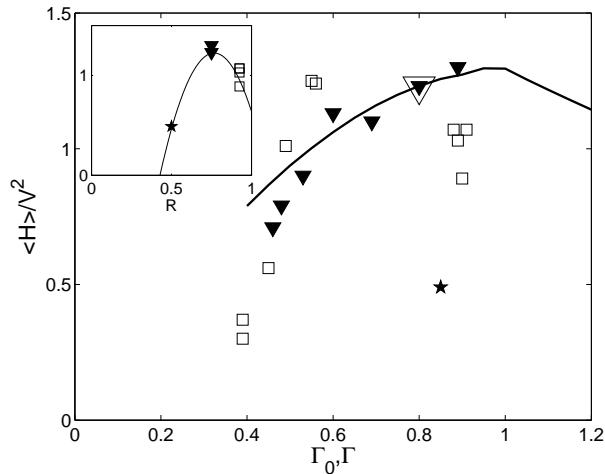


FIG. 13: Mean helicity at a given R_m ($\langle H \rangle / \mathcal{V}^2$) vs. poloidal over toroidal ratio. The $R = 0.75$ impeller series (\blacktriangledown) is plotted vs. Γ_0 . The large open symbol stands for TM73 at Γ_0 and the solid line stands for the same quantity plotted vs. numerical variation of TM73 velocity field (Γ). We also plot $\langle H \rangle / \mathcal{V}^2$ vs. Γ_0 for the $R = 0.5$ (\star) and $R = 0.925$ (\square) impellers. The inset presents $\langle H \rangle / \mathcal{V}^2$ vs. impeller radius R for impellers of $0.8 \lesssim \Gamma_0 \lesssim 0.9$.

As far as the optimal value toward dynamo action for the ratio Γ (close to $0.7 - 0.8$, depending on w) is lower than 1, the best velocity field is not absolutely helicity-maximizing. In other words, the best dynamo flow contains more toroidal velocity than the best helical flow. As shown by Leprovost [41], one can interpret the optimal Γ as a quantity that maximizes the product of mean helicity by a measure of the ω -effect, *i.e.*, the product $\langle H \rangle \langle T \rangle \sim \langle P \rangle \langle T \rangle^2$.

IV. IMPACT OF A CONDUCTING LAYER ON THE NEUTRAL MODE AND THE ENERGY BALANCE FOR THE VKS2 OPTIMIZED VELOCITY FIELD

In this section, we deal with the mean velocity field produced between two counterrotating TM73 impellers in a cylinder of aspect ratio $\frac{H_c}{R_c} = 1.8$, like the first experimental configuration chosen for the VKS2 experiment. See Table I for the characteristics of this impeller, and Fig. 2 for a plot of the mean velocity field. We detail the effects of adding a static layer of conductor surrounding the flow and compare the neutral mode structures, the magnetic energy and current density spatial repartition for this kinematic dynamo.

A. Neutral mode for $w = 0$

Without conducting layer, this flow exhibits dynamo action with a critical magnetic Reynolds number $R_m^c = 180$. The neutral mode is stationary in time and has a $m = 1$ azimuthal dependency. In Fig. 14, we plot an isodensity surface of the magnetic energy (50% of the maximum) in the case $w = 0$ at $R_m = R_m^c = 180$. The field concentrates near the axis into two twisted banana-shaped regions of strong axial field. Near the interface between the flow and the outer insulating medium, there are two small sheets located on both sides of the plane $z = 0$ where the magnetic field is almost transverse to the external boundary and dipolar. The topology of the neutral mode is very close to those obtained by Marié *et al.* [22] with different impellers, and to those obtained on analytical $s_2^0 t_2^0$ -like flows in a cylindrical geometry with the previously described Galerkin analysis [39].

In Fig. 15 we present sections of the \mathbf{B} and \mathbf{j} fields, $\mathbf{j} = \nabla \times \mathbf{B}$ being the dimensionless current density. The scale for \mathbf{B} is chosen such as the magnetic energy integrated over the volume is unity. Since the azimuthal dependency is $m = 1$, two cut planes are sufficient to describe the neutral mode. In the bulk where twisted-banana-shaped structures are identified, we note that the toroidal and poloidal parts of \mathbf{B} are of the same order of magnitude and that \mathbf{B} concentrates near the axis, where it experiences strong stretching due to the stagnation point in the velocity field. Around the center of the

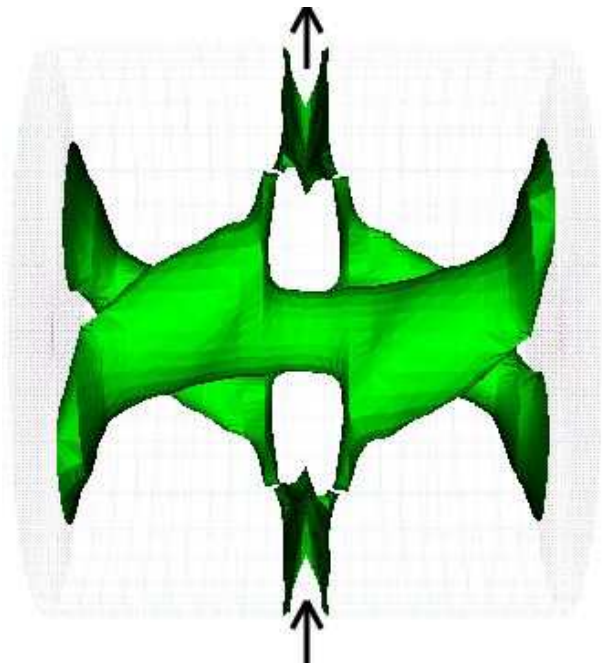


FIG. 14: Isodensity surface of magnetic energy (50% of the maximum) for the neutral mode without conducting layer ($w = 0$). Cylinder axis is horizontal. Arrows stand for the external dipolar field source regions.

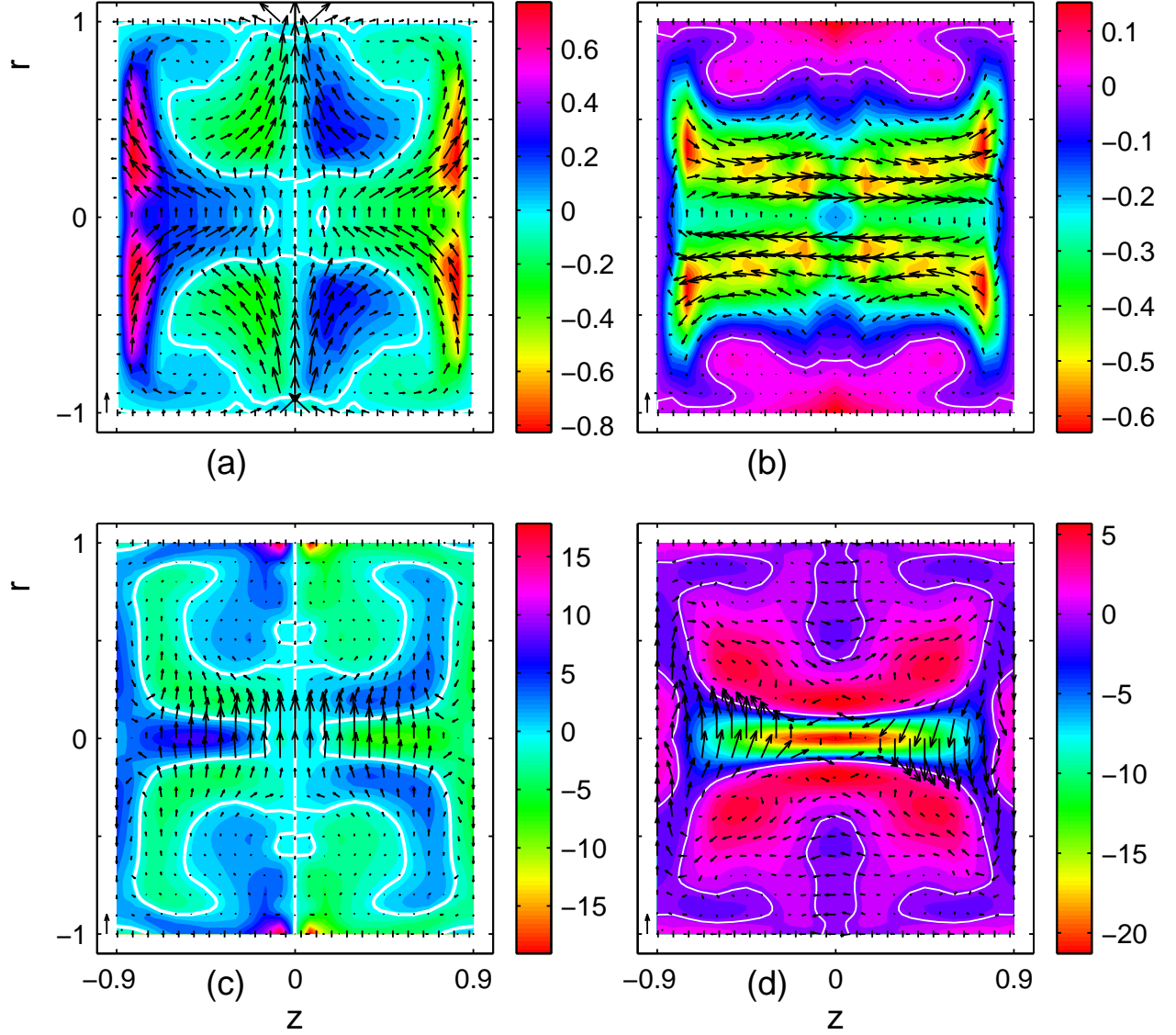


FIG. 15: Meridian sections of \mathbf{B} and \mathbf{j} fields for the neutral mode with $w = 0$. \mathbf{B} is divided by the total magnetic energy. Arrows correspond to components lying in the cut plane, and color code to the component transverse to the cut plane. A unit arrow is set into each figure lower left corner. (a): \mathbf{B} field, $\theta = 0$. (b) \mathbf{B} field, $\theta = \frac{\pi}{2}$. (c): \mathbf{j} field, $\theta = 0$. (d): \mathbf{j} field, $\theta = \frac{\pi}{2}$.

flow recirculation loops ($r \simeq 0.7$ and $z \simeq \pm 0.5$ see Fig. 2) we note a low level of magnetic field: it is expelled from the vortices. Close to the outer boundary, we mainly observe a strong transverse dipolar field (Fig. 15 upper-left) correlated with two small loops of very strong current density \mathbf{j} (Fig. 15 lower-left). These current loops seem constrained by the boundary, and might dissipate great amount of energy by Joule effect (see discussion below).

B. Effects of the conducting layer

As indicated in the first section, the main effect of adding a conducting layer is to strongly reduce the

threshold. In Fig. 16, we plot the critical magnetic Reynolds number for increasing values of the layer thickness. The reduction is important: the threshold is already divided by 4 for $w = 0.4$ and the effects tends to saturate exponentially with a characteristic thickness $w = 0.14$ (fit in Fig. 16), as observed for an α^2 -model of the Karlsruhe dynamo by Avalos *et al.* [43]. Adding the layer also modifies the spatial structure of the neutral mode: isodensity surface for $w = 0.6$ is plotted in Fig. 17 with the corresponding sections of \mathbf{B} and \mathbf{j} fields in Fig. 18. The two twisted bananas of axial field are still present in the core, but the sheets of magnetic energy near the $r = 1$ boundary strongly develop. Instead of thin folded sheets on both sides of the equatorial plane,

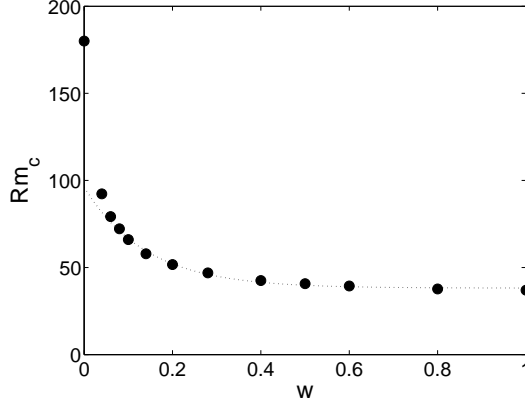


FIG. 16: Critical magnetic Reynolds number vs layer thickness w . TM73 velocity field. Fit: $R_m^c(w) = 38 + 58 \exp(-\frac{w}{0.14})$ for $w \geq 0.08$.

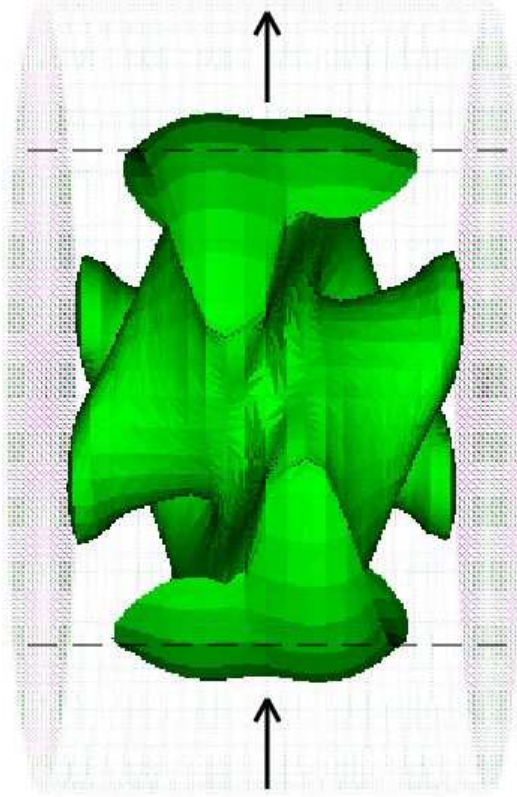


FIG. 17: Isodensity surface of magnetic energy (50% of the maximum) for the neutral mode with $w = 0.6$.

the structures unfold and grow in the axial and azimuthal directions to occupy a wider volume and extend on both sides of the flow/conducting-layer boundary $r = 1$. This effect is spectacular and occurs even for low values of w .

Small conducting layers are a challenge for numerical calculations: as far as the measured tangential velocity at the wall is not zero, adding a layer of conductor at

rest gives rise to a strong velocity shear, which in practice needs at least 10 grid points to be represented. The maximal grid width used is 0.005: the minimal non-zero w is thus $w = 0.05$. The exponential fit in Fig. 16 is relevant for $w \gtrsim 0.1$. We can wonder if the departure from exponential behavior is of numerical origin, or corresponds to a cross-over between different dynamo processes.

The analysis of \mathbf{B} and \mathbf{j} profiles in Fig. 18 first reveals smoother \mathbf{B} -lines and much more homogeneous a repartition for the current density. The azimuthal current loops responsible for the transverse dipolar magnetic field now develop in a wider space (Fig. 18 lower-left). Two poloidal current loops appear in this plane, closing in the conducting shell. These loops are responsible for the growth of the azimuthal magnetic field at $r = 1$ (Fig. 18 upper-left). Changes in the transverse plane ($\theta = \frac{\pi}{2}$) are less spectacular. As already stated in Refs. [42, 43], the positive effect of adding a layer of stationary conductor may reside in the subtle balance between magnetic energy production and Ohmic dissipation.

C. Energy balance

In order to better characterize which processes lead to dynamo action in a von Kármán flow, we will now look at the energy balance equation: let us first separate the whole space into three domains.

- $\Omega_i : 0 < r < 1$ (inner flow domain)
- $\Omega_o : 1 < r < 1 + w$ (outer stationary conducting layer)
- $\Omega_\infty : r > 1 + w$ (external insulating medium)

In any conducting domain Ω_α , we write the energy balance equation:

$$\frac{\partial}{\partial t} \int_{\Omega_\alpha} \mathbf{B}^2 = R_m \int_{\Omega_\alpha} (\mathbf{j} \times \mathbf{B}) \cdot \mathbf{V} - \int_{\Omega_\alpha} \mathbf{j}^2 + \int_{\partial\Omega_\alpha} (\mathbf{B} \times \mathbf{E}) \cdot \mathbf{n}$$

The term in the left part of the equation is the temporal variation of the magnetic energy E_{mag} . The first term in the right part of the equation corresponds to the source term which writes as a work of the Lorentz force. It exists only in Ω_i and is denoted W . The second term is the Ohmic dissipation D , and the last term is the Poynting vector flux P which vanishes at infinite r .

We have checked our computations by reproducing the results of Kaiser and Tilgner [42] on the Ponomarenko flow.

At the dynamo threshold, integration over the whole space gives

$$0 = W - D_o - D_i$$

In Fig. 19, we plot the integrands of W and D at the threshold for dynamo action, normalized by the total

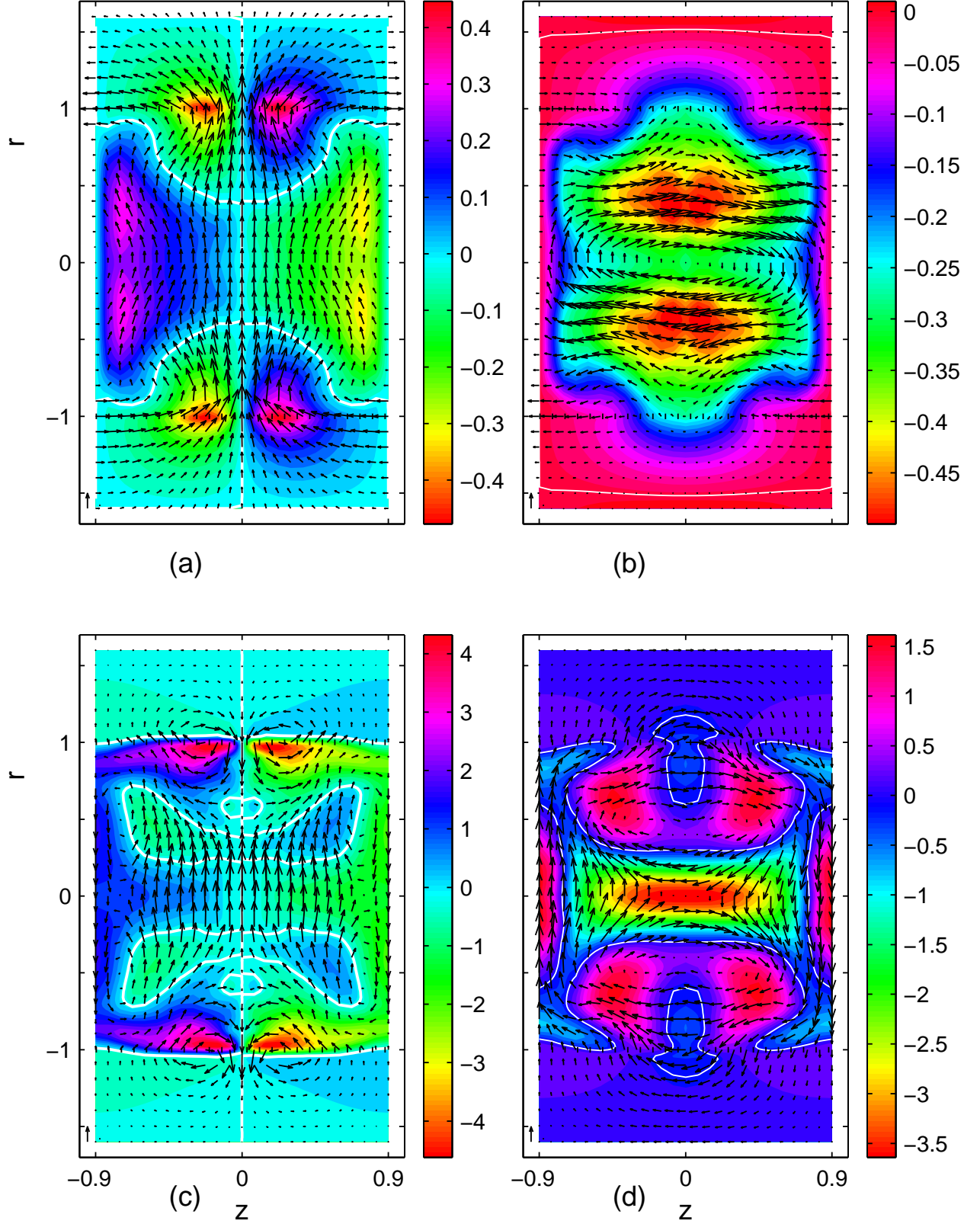


FIG. 18: Meridian sections of \mathbf{B} and \mathbf{j} fields for the neutral mode with $w = 0.6$. \mathbf{B} is divided by the total magnetic energy. Arrows correspond to components lying in the cut plane, and color code to the component transverse to the cut plane. A unit arrow is set into each figure lower left corner. (a): \mathbf{B} field, $\theta = 0$. (b) \mathbf{B} field, $\theta = \frac{\pi}{2}$. (c): \mathbf{j} field, $\theta = 0$. (d): (c): \mathbf{j} field, $\theta = \frac{\pi}{2}$.

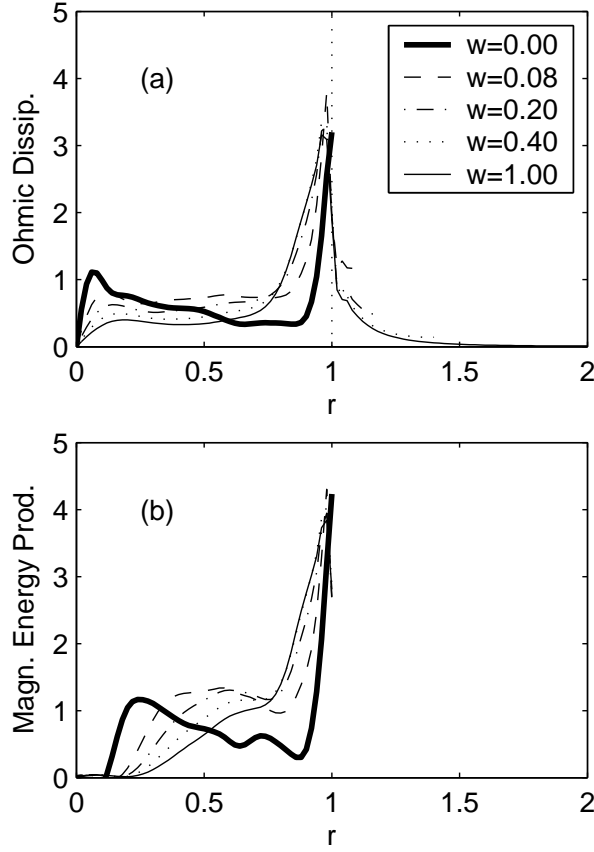


FIG. 19: (a): radial profile of Ohmic dissipation integrated over θ and z : $\int_0^{2\pi} \int_{-0.9}^{0.9} r \mathbf{j}^2(r) dz d\theta$ for increasing values of w . (b): radial profile of magnetic energy production integrated over θ and z : $\int_0^{2\pi} \int_{-0.9}^{0.9} r ((\mathbf{j} \times \mathbf{B}) \cdot \mathbf{V})(\mathbf{r}) dz d\theta$ for increasing values of w .

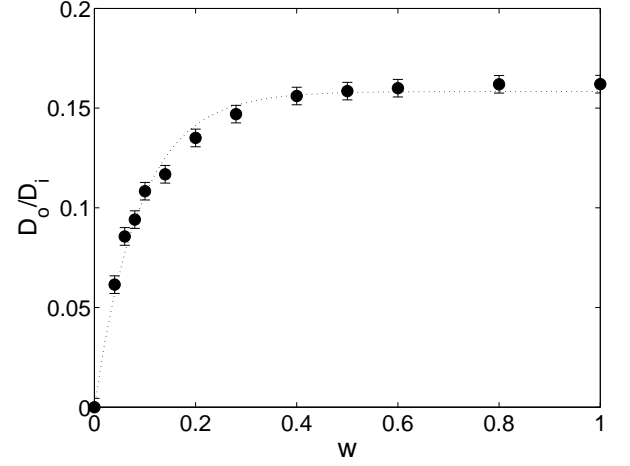


FIG. 20: Ratio of the integrated dissipation in the outer region and in the inner region $\frac{D_o}{D_i}$ vs w . Fit: $\frac{D_o}{D_i}(w) = 0.16 (1 - \exp(-\frac{w}{0.089}))$.

instantaneous magnetic energy, as a function of radius r for various w . For $w = 0$, both the production and dissipation mostly take place near the wall between flow and the insulating medium ($r = 1$), which could not have been guessed from the cuts of \mathbf{j} and \mathbf{B} in figure 15: the $w = 0$ curve in Fig. 19 has two bumps. The first one at $r \simeq 0.1$ corresponds to the twisted bananas, while the second is bigger and is localized near the flow boundary $r = 1$. A lot of current should be dissipated at the conductor-insulator interface due to the “frustration” of the transverse dipole. This can explain the huge effect of adding a conducting layer at this interface: the “strain concentration” is released when a conducting medium is added. So if we increase w , the remaining current concentration at $r = 1 + w$ decreases very rapidly to zero, which explains the saturation of the effect. In the mean time, the curves collapse on a single smooth curve, both for the dissipation and the production (solid black curves in Fig. 19). For greater values of w , the production density and the dissipation in the core of the flow $r < 0.2$ are smaller, whereas a peak of production and dissipation is still visible at the flow-conducting shell interface $r = 1$. The conducting layer does not spread but reinforces the localization of the dynamo process at this interface. This can help us to understand the process which rises the dynamo in a von Kármán type flow.

Let us now look at the repartition between the dissipation integrated over the flow D_i and the dissipation integrated over the conducting shell D_o (Fig. 20). The ratio D_o/D_i increases monotonically with w and then saturates to 0.16. This ratio remains small, which confirms the results of Avalos *et al.* [43] for a stationary dynamo. We conclude that the conducting layer existence—allowing currents to flow—happens to be more important than the relative amount of Joule energy dissipated in this layer.

D. Neutral mode structure

From the numerical results presented above in this section, we consider the following questions : Is it possible to identify typical structures in the eigenmode of the von Kármán dynamo ? If yes, do these structure play a role in the dynamo mechanism ? We have observed magnetic structures in the shape of bananas and sheets (see Figs. 14 and 17). In the center of the flow volume, there is an hyperbolic stagnation point equivalent to “ α -type” stagnation points in ABC-flows (with equal coefficients) [44]. In the equatorial plane at the boundary the merging of the poloidal cells remembers “ β -type” stagnation points in ABC-flows. In such flows, the magnetic field is organized into cigars along the α -type stagnation points and sheets on both sides of the β -type stagnation points [45]: this is very similar to the structure of the neutral mode we get for $w = 0$ (Fig. 14). We also performed magnetic induction simulations with an imposed axial field for the poloidal part of the flow alone. We obtain a strong axial stretching: the central stagnation point could be responsible for the growth of the bananas/cigars, which are twisted by the axial differential rotation after. One should nevertheless not forget that real instantaneous flows are highly turbulent, and that such peculiar stagnation points of the mean flow are especially sensitive to fluctuations.

The presence of the conducting layer introduces new structures in the neutral mode (see Figs. 14, 17 and 15, 18). In order to complete our view of the fields in the conducting layer, we plot them on the $r = 1$ cylinder for $w = 0.6$ (Fig. 21). As for $w = 0$, the dipolar main part of the magnetic field gets radially into the flow volume at $\theta = \pi$ and exits at $\theta = 0$ (Fig. 21 up). However, looking around $z = 0$, we observe that a part of this magnetic flux is azimuthally diverted in the conducting shell along the flow boundary. This effect does not exist without conducting shell: the outer part of the dipole is anchored in the stationary conducting layer.

Another specific feature is the anti-colinearity of the current density \mathbf{j} with \mathbf{B} at $(z = 0; \theta = 0, \pi; r = 1)$, which could remind an “ α ”-effect. However, while the radial magnetic field is clearly due to a current loop (arrows in the center of Fig. 21 down), j_r is not linked to a \mathbf{B} -loop (Fig. 21 up), which is not obvious from Fig. 18. Thus, the anti-colinearity is restricted to single points $(z = 0; \theta = 0, \pi; r = 1)$. We have checked this, computing the angle between \mathbf{j} and \mathbf{B} : the isocontours of this angle are very complex and the peculiar values corresponding to colinearity or anti-colinearity are indeed restricted to single points.

E. Dynamo threshold reduction factor

We have shown that the threshold for dynamo action is divided by four when adding a conducting layer of thickness $w = 0.4$. This effect is very strong. Following Avalos

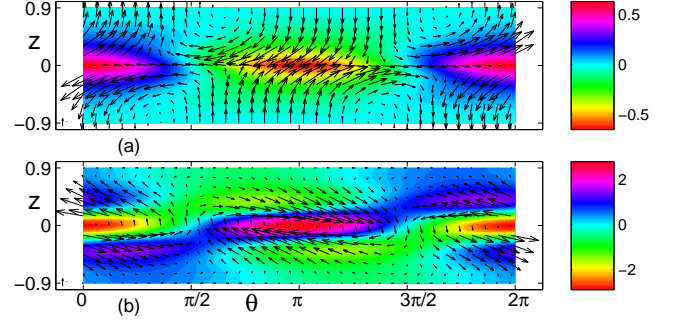


FIG. 21: (a): (resp. (b)) \mathbf{B} (resp. \mathbf{j}) field at $r = 1$ for $w = 0.6$. Color code corresponds to B_r (resp. j_r) and arrows to B_z and B_θ (resp. j_z and j_θ).

and Plunian [43], let us compare the threshold reduction factor $\Lambda = 1 - \frac{R_m^c(w)}{R_m^c(w=0)}$ for various kinematic dynamos. The threshold reduction for TM73-flow ($\Lambda = 0.78$) is much higher than for the Karlsruhe ($\Lambda = 0.11$) and Riga ($\Lambda = 0.56$) dynamos. Reduction rate can also be radically different between model flows: the α^2 -model for Karlsruhe dynamo gives a low- R_m^c -dynamo for $w = 0$ and benefits very few of a finite w ($\Lambda = 0.11$), while the Ponomarenko flow does not lead to dynamo action without conducting layer ($\Lambda = 1$). The reduction factors considered above are maximal values obtained either for high w in stationary dynamos or for the optimal w in oscillatory dynamos [42, 43].

In order to understand why Λ is so high for our TM73-flow, we propose to compare our experimental flow with an optimal analytical model-flow proposed by Marié, Normand and Daviaud [39] in the same geometry. The Galerkin method used by these authors does not allow to study the effect of a conducting layer. We thus perform kinematic dynamo simulations with our usual approach, and then study the effects of adding a conducting layer on the following velocity field for $\epsilon = 0.7259$ corresponding to $\Gamma = 0.8$ [29, 39]:

$$\begin{aligned} v_r &= -\frac{\pi}{2}r(1-r)^2(1+2r)\cos(\pi z) \\ v_\theta &= 4\epsilon r(1-r)\sin(\pi z/2) \\ v_z &= (1-r)(1+r-5r^2)\sin(\pi z) \end{aligned} \quad (2)$$

The kinematic dynamo threshold is found at $R_m^c = 58$ for $w = 0$, in good agreement with the galerkin analysis. With a $w = 1$ conducting layer, we get a low $\Lambda = 0.26$ reduction rate, *i.e.* $R_m^c = 43$, close to the TM73 threshold for $w = 1$: $R_m^c = 37$. The threshold reduction is also found to show an exponential behavior with w , of characteristic thickness 0.20, as in Fig. 16.

Let us describe the model flow features represented in Fig. 7 (bottom). The velocity is very smooth at the cylindrical boundary: the toroidal velocity is maximum at $r = 0.5$ and slowly decreases to zero at $r = 1$. The

poloidal recirculation loops are centered at $r_p = 0.56$ and the axial velocity also decreases slowly to zero at the cylindrical boundary. Thus, the mass conservation requires the axial velocity to be much higher in the central disk ($0 < r < r_p$) than outside. These constraints make analytical models somewhat different from experimental mean flows (Fig. 7). In particular, high kinetic Reynolds numbers forbid smooth velocity decrease near boundaries. This explains why experimental flows do not lead to low thresholds unless a conducting layer is added.

We now consider the effect of a conducting shell on the model flow eigenmode structure. First note that without conducting shell, the model neutral mode structure is already very similar to that of TM73 with conducting shell: the transverse dipole is not confined into thin sheets but develops into wider regions connected to bananas of axial field in the center. Adding the conducting layer mainly lets the neutral mode structure unchanged and thus quantitatively reduces its impact compared to the experimental case.

Finally, from the very numerous simulations of experimental and model von Kármán flows performed, we conclude that the adjunction of a static conducting layer to experimental flows makes the eigenmode geometry closer to optimal model eigenmodes, and critical R_m^c get closer to moderate values (typically 50). It may thus be conjectured that the puzzling sensitivity of dynamo threshold to flow geometry is lowered when a static layer is present. We conclude this feature renders the dynamo more robust to flow topology details. This could also act favorably in the nonlinear regime.

V. CONJECTURES ABOUT DYNAMO MECHANISMS

In this paragraph, we intend to relate the results of the optimization process to some more elementary mechanisms. As emphasized in the Introduction, there is no sufficient condition for dynamo action and although numerical examples of dynamo flows are numerous, little is known about the effective parameters leading to an efficient energy conversion process. For example, the classical α and axial ω mechanisms have been proposed to be the main ingredients of the von Kármán dynamo [19]. Our starting point is the observation that dynamo action results from a constructive coupling between magnetic fields components due to velocity gradients, which, in the present axisymmetric case, reduce to derivatives with respect to r (radial gradients) and to z (axial gradients). The gradients of azimuthal velocity generate a toroidal field from a poloidal one (ω -effect [1]), while regeneration of the poloidal field is generally described as resulting from an helicity effect (denoted α -effect if scale separation is present [26]). How do these general considerations apply to the present flow? As in the Sun, which shows both a polar-equatorial differential rotation and a tachocline transition, our experimental flow fields

present azimuthal velocity shear in axial and radial directions (see Fig. 2). So, we will consider below the role of both axial and radial ω -effect.

We will discuss these mechanisms and then suggest that, for a flow surrounded by a static conducting layer, the dynamo mechanism is based on the presence of a strong velocity shear (at the boundary layer $r = 1$) which lies in this case in the bulk of the overall electrically conducting domain.

A. Axial ω -effect

Induction simulations performed with the toroidal part of the velocity show an axial ω -effect which converts an imposed axial field into toroidal field through $\partial v_\theta / \partial z$. Such a R_m -linear effect has been evidenced in VKS1 experiment [20]. This effect concentrates around the equatorial shear layer ($z = 0$) as visible in Fig. 2. Thus, we can think that the axial ω -effect is involved in the dynamo process: for dynamo action to take place, there is a need for another process to convert toroidal magnetic field into poloidal field.

B. α -effect, helicity effect

R_m -non-linear conversion from transverse to axial magnetic field has also been reported in VKS1 experiment [21]. This effect is not the usual scale-separation α -effect [26] and has been interpreted as an effect of the global helicity as reported by Parker [40] (in the following, it will be denoted “ α ”-effect). We believe it to take place in the high kinetic helicity regions of the flow (see Fig. 12).

C. Is an “ α ” ω mechanism relevant?

Bourgoin *et al.* [46] performed a study of induction mechanisms in von Kármán-type flows, using a quasi-static iterative approach. They show that “ α ” ω dynamo action, seen as a three-step loop-back inductive mechanism, is possible, but very difficult to obtain, fields being widely expelled by the vortices. The authors highlight the fact that the coupling between the axial ω -effect and the “ α ”-effect is very inefficient for our velocity fields, because of the spatial separation of these two induction effects. Our observations of the velocity and helicity fields confirm this separation.

The authors also discovered an induction effect — the BC-effect — related to the magnetic diffusivity discontinuity at the insulating boundary that could be invoked in the dynamo mechanism. This BC-effect, illustrated on our TM73-velocity field (Fig. 14 in Ref. [46]), is enhanced in the case of strong velocity and vorticity gradients at the boundaries, characteristic of high Reynolds number flows. So, we are convinced that for experimental flow

fields at $w = 0$, the BC-effect helps the dynamo. This is coherent with our observations of high tangential current density near the boundaries and high magnetic energy production at $r = 1$ even for $w = 0$ (Fig. 19). Such a current sheet formation and BC-effect was reported by Bullard and Gubbins [24].

When a large layer of sodium at rest is added, the BC-effect vanishes because the conductivity discontinuity occurs at $r = 1 + w$ while the currents still concentrate at the flow boundary $r = 1$. However, with a conducting layer, we have presented many features favoring the dynamo: in the next paragraph, we propose a possible origin for this conducting-layer effect.

D. Radial ω -effect, boundary layers and static shell

With a layer of steady conducting material surrounding the flow, we note the occurrence of two major phenomena:

- the possibility for currents to flow freely in this shell (Fig. 19),
- the presence of a very strong velocity shear localized at the boundary layer which now lies in the bulk of the electrically conducting domain.

Let us again consider the shape of the velocity shear. Any realistic (with real hydrodynamical boundary conditions) von Kármán flow obviously presents negative gradients of azimuthal velocity $\partial v_\theta / \partial r$ between the region of maximal velocity and the flow boundary. This region can be divided into two parts: a smooth decrease in the bulk ($R \lesssim r \lesssim 1$) and a sharp gradient in the boundary layer at $r = 1$ (Fig. 7).

These gradients are responsible for a radial ω -effect, producing B_θ with B_r , in both insulating and conducting cases. However, without conducting layer, only the smooth part of the gradient which lies in the bulk will be efficient for dynamo action. Indeed, owing to the huge value of the kinetic Reynolds number and the very small value of the magnetic Prandtl number, the sharp boundary layer gradient is confined in a tiny domain, much smaller than the magnetic variation scale. No significant electrical currents can flow in it and we did not resolve this boundary layer with the numerical code: it is totally neglected by our approach.

The role of both types of gradients is illustrated by the observation (Fig. 7, left) of impellers of large radius ($R = 0.925$). For such impellers there is almost no departure from solid body rotation profiles in the flow region and these impellers lead to dynamo action only with conducting shell [22], *i.e.*, due to the sharp gradient. On the other hand, our $R = 0.75$ selected impellers present a stronger bulk-gradient and achieve dynamo in both cases.

Actually, the way we numerically modeled the von Kármán flow surrounded by a static conducting layer—considering an equivalent fluid system in which the

boundary layer appears as a simple velocity jump in its bulk—is coherent with the problem to solve. The velocity jump, just as any strong shear, is a possible efficient source for the radial ω -effect.

E. A shear and shell dynamo ?

We pointed out above that the regions of maximal helicity (the “ α ”-effect sources, see Fig. 12) are close to those of radial shear where radial ω -effect source term takes place. Dynamo mechanism could thus be the result of this interaction. So, in the absence of a static shell, one can suppose that the dynamo arises from the coupling of “ α ”-effect, ω -effect and the BC-effect [46]. With a static conducting layer, as explained above, the radial ω -effect is especially strong: the radial dipole, anchored in the conducting layer and azimuthally stretched by the toroidal flow (see Fig. 21) is a strong source of azimuthal field. This effect coupled with the “ α ”-effect could be at the origin of the dynamo.

For small conducting layer thickness w , one could expect a cross-over between these two mechanisms. In fact, it appears that the decrease of R_m^c (Fig. 16) with the conducting shell thickness w is very fast between $w = 0$ and $w = 0.08$ and is well fitted for greater w by an exponential, as in Ref. [43]. We can also note that for typical $R_m = 50$, the dimensionless magnetic diffusion length $R_m^{-1/2}$ is equal to 0.14. This value corresponds to the characteristic length of the R_m^c decrease (Fig. 16) and is also close to the cross-over thickness and characteristic lengths of the Ohmic dissipation profiles (Figs. 19, top and 20).

We propose to call the mechanism described above a “shear and shell” dynamo. This interpretation could also apply to the Ponomarenko screw-flow dynamo which also merely relies on the presence of an external conducting medium.

VI. CONCLUSION

We have selected a configuration for the mean flow feasible in the VKS2 liquid sodium experiment. This mean flow leads to kinematic dynamo action for a critical magnetic Reynolds number below the maximum achievable R_m . We have performed a study of the relations between kinematic dynamo action, mean flow features and boundary conditions in a von Kármán-type flow.

The first concluding remark is that while the dynamo without static conducting shell strongly depends on the bulk flow details, adding a stationary layer makes the dynamo threshold more robust. The study of induction mechanisms in 3D cellular von Kármán type flows performed by Bourgoïn *et al.* [46] suggests that this sensitivity comes from the spatial separation of the different induction mechanisms involved in the dynamo process: the loop-back between these effects cannot overcome the

expulsion of magnetic flux by eddies if the coupling is not sufficient. Secondly, the role of the static layer is generally presented as a possibility for currents to flow more freely. But, instead of a spreading of the currents, the localization at the boundary of both magnetic energy production and dissipation (Fig. 19) appears strongly reinforced. Actually, strong shears in the bulk of the electrically conducting domain imposed by material boundaries are the dominating sources of dynamo action. They result in a better coupling between the inductive mechanisms. We also notice that there seems to be a general value for the minimal dynamo threshold (typically 50) in our class of flows, for both best analytical flows and experimental flows with static conducting layer.

Although the lowering of the critical magnetic Reynolds number due to an external static envelope seems to confirm previous analogous results [16, 42, 43], it must not be considered as the standard and general answer. In fact, in collaboration with Frank Stefani and Mingtian Xu from the Dresden MHD group, we are presently examining how such layers, when situated at

both flat ends, *i.e.*, besides the propellers, may lead to some increase of the critical magnetic Reynolds number. This option should clearly be avoided to optimize fluid dynamos similar to VKS2 configuration. However, a specific study of this later effect may help to better understand how dynamo action, which is a global result, relies also on the mutual effects of separated spatial domains with different induction properties.

Acknowledgments

We would like to thank the other members of the VKS team, M. Bourgoin, S. Fauve, L. Marié, P. Odier, F. Pétrélis, J.-F. Pinton and R. Volk, as well as B. Dubrulle, N. Leprovost, C. Normand, F. Plunian and F. Stefani for fruitful discussions. We are indebted to V. Padilla and C. Gasquet for technical assistance. We thank the GDR dynamo for support.

-
- [1] H.K. Moffatt, *Magnetic Field Generation in Electrically Conducting Fluids* (Cambridge University Press, Cambridge, England, 1978).
 - [2] A. Gailitis, O. Lielausis, S. Dement'ev, E. Platadis, & A. Cifersons, "Detection of a Flow Induced Magnetic Field Eigenmode in the Riga Dynamo Facility," *Phys. Rev. Lett.* **84**, 4365 (2000).
 - [3] R. Stieglitz & U. Müller, "Experimental demonstration of a homogeneous two-scale dynamo," *Phys. Fluids* **13**, 561 (2001).
 - [4] A. Gailitis, O. Lielausis, E. Platadis, S. Dement'ev, A. Cifersons, G. Gerbeth, T. Gundrum, F. Stefani, M. Christen & G. Will, "Magnetic Field Saturation in the Riga Dynamo Experiment," *Phys. Rev. Lett.* **86**, 3024 (2001).
 - [5] A. Gailitis, O. Lielausis, E. Platadis, G. Gerbeth, & F. Stefani, "Colloquium: Laboratory experiments on hydromagnetic dynamos," *Rev. Mod. Phys.* **74**, 973 (2002).
 - [6] U. Müller, R. Stieglitz & S. Horanyi, "A two-scale hydromagnetic dynamo experiment," *J. Fluid Mech.* **498**, 361-71 (2004).
 - [7] F. Stefani, G. Gerbeth, & A. Gailitis, "Velocity profile optimization for the Riga dynamo experiment," *Transfer Phenomena in Magnetohydrodynamic and Electroconducting Flows*, pp31-44, A. Alemany Ph. Marty, J.-P. Thibault Eds., Kluwer Academic Publishers, Dordrecht, The Netherlands (1999).
 - [8] A. Tilgner, "Numerical simulation of the onset of dynamo action in an experimental two-scale dynamo," *Phys. Fluids* **14**, 4092 (2002).
 - [9] A. Tilgner & F. H. Busse, "Simulation of the bifurcation diagram of the Karlsruhe dynamo," *magnetohydrodynamics*, **38**, 35-40 (2002).
 - [10] F. Plunian & K.-H. Rädler, "Subharmonic dynamo action in the Roberts flow," *Geophys. Astrophys. Fluid Dyn.* **96**, 115 (2002).
 - [11] D. Sweet, E. Ott, J. M. Finn, T. M. Antonsen & D. P. Lathrop, "Blowout bifurcations and the onset of magnetic activity in turbulent dynamos," *Phys. Rev. E* **63**, 066211 (2001).
 - [12] A. Gailitis, O. Lielausis, E. Platadis, G. Gerbeth & F. Stefani, "The Riga Dynamo Experiment," *Surveys in Geophysics* **24**, 247 (2003).
 - [13] F. Cattaneo, D. W. Hughes, & E.-J. Kim, "Suppression of Chaos in a Simplified Nonlinear Dynamo Model," *Phys. Rev. Lett.* **76**, 2057 (1996).
 - [14] F. Pétrélis & S. Fauve, "Saturation of the magnetic field above the dynamo threshold," *Eur. Phys. J. B* **22**, 273 (2001).
 - [15] Y. Ponty, H. Politano, & J.-F. Pinton, "Simulation of Induction at Low Magnetic Prandtl Number," *Phys. Rev. Lett.* **92**, 144503 (2004).
 - [16] F. Pétrélis, *Effet dynamo: Etude des mécanismes d'instabilité et de saturation du champ magnétique*, PhD. Thesis, Université Paris VI, 2002.
 - [17] S. Fauve & F. Pétrélis, *The dynamo effect*, in *Peyresq Lectures on Nonlinear Phenomena, Vol. II*, J.-A. Sepulchre Ed., World Scientific, Singapore (2003).
 - [18] *Dynamo and Dynamics, a Mathematical Challenge, Cargèse (France) August 21-26, 2000*, edited by P. Chossat, D. Armbruster, I. Oprea, NATO ASI series (Kluwer Academic Publishers, 2001).
 - [19] L. Marié, F. Pétrélis, M. Bourgoin, J. Burguete, A. Chiffaudel, F. Daviaud, S. Fauve, P. Odier & J.-F. Pinton, "Open questions about homogeneous fluid dynamos: the VKS experiment," *Magnetohydrodynamics* **38**, 156-169 (2002).
 - [20] M. Bourgoin, L. Marié, F. Pétrélis, C. Gasquet, A. Guigon, J.-B. Luciani, M. Moulin, F. Namer, J. Burguete, A. Chiffaudel, F. Daviaud, S. Fauve, P. Odier, & J.-F. Pinton, "MHD measurements in the von Kármán sodium experiment," *Phys. Fluids* **14**, 3046 (2002).
 - [21] F. Pétrélis, M. Bourgoin, L. Marié, J. Burguete, A. Chiffaudel, F. Daviaud, S. Fauve, P. Odier & J.-F. Pinton,

- “Nonlinear magnetic induction by helical motion in a liquid sodium turbulent flow,” *Phys. Rev. Lett.* **90**, 174501 (2003).
- [22] L. Marié, J. Burguete, F. Daviaud & J. Léorat, “Numerical study of homogeneous dynamo based on experimental von Kármán type flows,” *Eur. Phys. J. B* **33**, 469 (2003).
- [23] N. L. Dudley & R. W. James, “Time-dependent kinematic dynamos with stationary flows,” *Proc. Roy. Soc. Lond. A* **425**, 407 (1989).
- [24] E. C. Bullard & D. Gubbins, “Generation of magnetic fields by fluid motions of global scale,” *Geophys. Astrophys. Fluid Dyn.* **8**, 43 (1977).
- [25] A.B. Reighard & M.R. Brown, “Turbulent conductivity measurements in a spherical liquid sodium flow,” *Phys. Rev. Lett.* **86**, 2794 (2001).
- [26] F. Krause & K. H. Rädler, *Mean field MHD and dynamo theory*, Pergamon press (1980).
- [27] L. Marié & F. Daviaud, “Experimental measurement of the scale-by-scale momentum transport budget in a turbulent shear flow,” *Phys. Fluids* **16**, 457 (2004).
- [28] C.B. Forest, R. O’Connell, R. Kendrick, E. Spence, and M.D. Nornberg, “Hydrodynamic and numerical modeling of a spherical homogeneous dynamo experiment,” *Magnetohydrodynamics* **38**, 107-120 (2002).
- [29] L. Marié, *Transport de moment cinétique et de champ magnétique par un écoulement tourbillonnaire turbulent: influence de la rotation*, PhD. thesis, Université Paris VII, 2003.
- [30] U. Frisch, *Turbulence - The legacy of A. N. Kolmogorov*, Cambridge University Press, New-York, (1995).
- [31] F. Ravelet, *Etude expérimentale de l’écoulement tourbillonnaire de von Kármán et application à l’effet dynamo*, M. S. thesis, Université Paris VI (2002).
- [32] J. Léorat, “Numerical Simulations of Cylindrical Dynamos: Scope and Method,” *Prog. Ser. Am. Inst. Astronautics and Aeronautics* **162**, 282 (1994).
- [33] E. Knobloch, “Symmetry and instability in rotating hydrodynamic and magnetohydrodynamic flows,” *Phys. Fluids* **8**, 1446 (1996).
- [34] E. C. Bullard & H. Gellman, “Homogeneous dynamos and terrestrial magnetism,” *Phil. Trans. Roy. Soc. A* **247**, 213 (1954).
- [35] G. E. Backus, “A class of self-sustaining dissipative spherical dynamos,” *Ann. Phys.* **4**, 372 (Leipzig 1958).
- [36] J. J. Love & D. Gubbins, “Dynamos driven by poloidal flow exist,” *Geophys. Res. Letters* **23**, 857 (1996).
- [37] M. R. E. Proctor, “An extension of the toroidal theorem,” *Geophys. Astrophys. Fluid Dynamics* **98**, 235 (2004).
- [38] M. Lesieur, *Turbulence in Fluids*, second revised edition, Kluwer academic publishers, Dordrecht (1990).
- [39] L. Marié, C. Normand & F. Daviaud, “Galerkin analysis of kinematic dynamos in von Kármán geometry,” submitted to *Phys. Fluids* (2004). First results can be found in [29].
- [40] E. N. Parker, “Hydromagnetic dynamo models,” *Astrophys. J.* **122**, 293 (1955).
- [41] N. Leprovost, *Influence des petites échelles sur la dynamique à grande échelle en turbulence magnétohydrodynamique*, PhD. thesis, Université Paris VI (2004).
- [42] R. Kaiser & A. Tilgner, “Kinematic dynamos surrounded by a stationary conductor,” *Phys. Rev. E* **60**, 2949 (1999).
- [43] R. Avalos-Zuniga & F. Plunian, “Influence of electromagnetic boundary conditions onto the onset of dynamo action in laboratory experiments,” *Phys. Rev. E* **68**, 066307 (2003).
- [44] S. Childress, A. D. Gilbert, *Stretch, Twist, Fold: The fast dynamo*, Springer Verlag (1995).
- [45] V. Archontis, S. B. F. Dorch, & A. Nordlund, “Numerical simulations of kinematic dynamo action,” *Astronomy and Astrophysics* **397**, 393 (2003).
- [46] M. Bourgoin, P. Odier, J.-F. Pinton & Y. Ricard, “An iterative study of time independent induction effects in magnetohydrodynamics,” *Phys. Fluids* **16**, 2529 (2004).

